Journal of Inorganic and General Chemistry
ZAAC
Zeitschrift für anorganische und allgemeine Chemie
DOI: 10.1002/zaac.201800421
ARTICLE

Exploring the Cu-In-S System under Solvothermal Conditions near the Composition $CuIn_5S_8$

Henning Lühmann,[a] Enrique Quiroga-González,[b] Lorenz Kienle,*[c] Viola Duppel,[d] Gero Neubüser,[c] and Wolfgang Bensch*[a]

Dedicated to Prof. Dr. T. Fässler on the Occasion of his 60th Birthday

Abstract. Solvothermal syntheses of copper-indium-sulfides performed with different Cu:In:S ratios afforded crystallization of nanocrystalline Cu-In-S phases with compositions close to $CuInS_2$, $CuIn_3S_5$, and $CuIn_7S_{11}$. Each sample shows a different and distinguishable morphology. The minority component $CuInS_2$ with wurtzite-type structure crystallizes as thin plates, which are preferably stacked parallel to black stacks. The component with composition $CuIn_3S_5$ forms isolated few nm thin layers being arranged like the petals of a flower growing from a common point. Finally, red $CuIn_7S_{11}$ is obtained as nanobelts with individual diameters of about 20 nm and lengths up to more than 1 µm. According to electron diffraction patterns and X-ray diffractometry the structures of $CuIn_3S_5$ and $CuIn_7S_{11}$ cannot be assigned to known bulk phases of the Cu-In-S system, however first structure models are proposed.

Introduction

Ternary Cu-In-S nanocrystals have been discussed in literature as suitable materials for high-efficiency solar cells[1,2] and as materials for solar energy conversion.[3–16] The most intensively studied phase of this ternary system is $CuInS_2$ (CIS). CIS is trimorphic crystallizing in the chalcopyrite- (CP), zincblende- (ZB), and wurtzite-type (WZ) structures.[17,18] In the ZB and WZ structures the cations are disordered leading to a more flexible stoichiometry compared to the CP phase with ordered occupancy of the cation positions. The compositional variability of CIS is large and for ZB CIS, Cu:In:S ratios ranging from $CuIn_{2.2}S_{3.8}$ to $Cu_3InS_{3.1}$ has been reported.[19] The sizes of crystalline domains in these materials vary from 3 to about 30 nm. While the WZ structure can be identified in X-ray powder patterns, distinguishing ZB from CP structure is not always easy, because in the nanoregime reflections are broadened and reflection intensities are low. CIS with the CP structure exhibits a direct bandgap of ca. 1.5 eV, which is ideal for solar energy conversion. More interestingly, the bandgap can be tuned between 1.7 and 3.3 eV for particles between 1 and 6 nm.[20,21] In addition, the bandgap can be altered by adjusting the chemical composition, i.e. Cu poor CIS nanoparticles have a larger bandgap.[22]

Compared to $CuInS_2$, the other phases in the Cu-In-S system, $CuIn_{2n+1}S_{3n+2}$ with n = 0, 1 and 2, have been less intensively studied. For $CuIn_3S_5$ the structure was reported as chalcopyrite-like with the tetragonal space group $P\bar{4}2c$[23] and may be regarded as an ordered defect compound. The formation of this compound was mainly observed in Cu-In-S thin films.[24–28] The optical properties and morphology of such films were studied by several groups.[29–31] Optical absorption spectra show two transitions, which was explained with the valence band to conduction band transition (E_g = 1.93 eV) and an indirect transition (E_g = 1.57 eV) due to band splitting by the crystal field.[30] The compound was also tested as photoelectrode material for photoelectrochemical water splitting due to the promising bandgap of 1.54 eV.[32] $CuIn_5S_8$ was reported to crystallize in the cubic space group $F\bar{4}3m$,[33] while in other studies a defect spinel-type structure was proposed with space group $Fd\bar{3}m$.[23,34] $CuIn_5S_8$ crystals with both S deficiency and S excess have been also grown from the melt and depending on the actual stoichiometry the electrical properties varied significantly.[35] Depending on the Cu/In ratio in $CuIn_5S_8$ the optical bandgap varies from 1.57 eV (Cu/In = 0.22) to 1.87 eV (Cu/In = 0.5).[36] Varying the Cu/In ratio in electrodeposited $CuIn_5S_8$ films led to crystallization of a phase pure material for Cu/In = 0.28, whereas all other samples were mixtures of $CuInS_2$/$CuIn_5S_8$ or $CuIn_5S_8$/In.[37] An interesting structural observation was reported for the series $(CuIn_5S_8)_{1-x}(In_2S_3)_x$, where all samples crystallized in $F\bar{4}3m$ with a linear expansion of the lattice parameter with increasing x.[38]

The latest compound reported in literature is $CuIn_7S_{11}$, which crystallizes as a defect spinel (space group: $Fd\bar{3}m$).[39] The optical bandgap of this material was measured on single

* Prof. Dr. L. Kienle
E-Mail: lk@tf.uni-kiel.de
* Prof. Dr. W. Bensch
E-Mail: wbensch@ac.uni-kiel.de
[a] Institut für Anorganische Chemie der Universität Kiel
Max-Eyth-Str.2
24119 Kiel, Germany
[b] Institute of Physics
Benemérita Universidad Autónoma de Puebla (BUAP)
Puebla, Mexico
[c] Institute for Material Science of the University of Kiel
Kaiserstr. 2
24143 Kiel, Germany
[d] Nanochemistry
Max Planck Institute for Solid State Research
Heisenbergstr. 1
70569 Stuttgart, Germany

crystals yielding E_g = 2.23 eV.[40] For $CuIn_7S_{11}$ films a significant dependence of the optical properties from the film thickness was observed with values for E_g = 2.30 eV (d = 460 nm) and E_g = 1.98 eV (d = 290 nm).[41]

Cu-In-S nanomaterials with distinct sizes and morphologies are synthesized mainly by using the hot-injection method in organic solvents containing capping molecules[42–47] under solvothermal conditions[48–53] or the so-called heating up methods.[54–58] In the overwhelming cases nano-crystalline Cu-In-S phases are obtained applying Cu and In salts either as dual sources or as single source.[59–65] From thiometalate chemistry it is well known that multinary compounds can be solvothermally prepared using the metals in the presence of elemental sulfur and basic media. Sulfur reacts in alkaline solution generating polysulfide species (besides different thiosulfates), which attack and dissolve the metals. This approach was applied for the synthesis of $CuInS_2$.[66] In this publication the authors used a 1:1:2 stoichiometric ratio for Cu:In:S and performed a solvothermal reaction at 280 °C for 48 h. The final product consisted of nanorods with a nearly stoichiometric composition in agreement with $CuInS_2$. This observation is somewhat surprising because a large amount of elemental sulfur is consumed by the reaction to polysulfide anions besides sulfite/thiosulfate anions in basic media.[67,68]

The main aims of all investigations in the references mentioned above were the syntheses of the known Cu-In-S phases and their characterization with respect to different physical and chemical properties. The In and S rich Cu-In-S phases were mainly synthesized as films or by reaction of the elements at elevated temperatures. Solvothermal approaches for the preparation of such phases are rare and solely salts of Cu and In were reacted in the presence of S-containing sources.

The aim of the presented investigation was the synthesis of $CuIn_5S_8$ applying Cu, In, and S as starting materials in ethylenediamine (en) as solvent. By systematic variation of the Cu:In:S ratio as 1.3:5:X with X = 8, 8.5, 9, and 9.5 but keeping the other synthesis parameters constant we were able to synthesize nanocrystalline materials with compositions close to $CuInS_2$ (wurtzite type structure), $CuIn_3S_5$ and $CuIn_7S_{11}$, all exhibiting different morphologies. The phase with composition $CuIn_3S_5$ occurred as intermediate during formation of $CuIn_7S_{11}$ as evidenced by long term syntheses. $CuIn_7S_{11}$ was obtained as bright red nanocrystals, whereas a phase pure product of $CuIn_3S_5$ could not be obtained. Herein we report the syntheses, structural analyses with X-ray powder diffraction and transmission electron microscopy, and the optical properties (UV/Vis spectroscopy) of the samples.

Experimental Section

The starting materials were elemental Cu, In, and S. Reproducible mixtures of optically identifiable phases were obtained using the following procedures: Elemental Cu (Alfa Aesar, 99.9 %), In (Alfa Aesar, 99.9 %), and S (Alfa Aesar, 99.9 %) in a molar proportion of 1.3:5:X, (X = 8–9.5) (total amount: ca. 0.1 g) were mixed with 5 mL of ethylenediamine in a 35 mL Teflon-lined stainless steel autoclave. The sealed vessel was heated at 220 °C for 5 d in the first series of syntheses. Selected syntheses were also extended up to 20 d. After cooling down to room temperature, the product was filtered off, and washed with water, ethanol, and acetone. The manual separation of black, orange, and red crystals is a very difficult task because they are attached to each other preventing a full separation.

X-ray powder patterns were collected with a PANalytical X'pert-PRO diffractometer in reflection mode with a resolution of 0.026° (Cu-K_α radiation, λ = 1.54056).

The morphology of the compounds was analyzed by SEM (Philips ESEM XL30, Zeiss Gemini FESEM). Microstructure and composition were determined by Transmission Electron Microscopy (TEM) utilizing high resolution transmission electron microscopy (HRTEM), selected area electron diffraction (SAED) and energy dispersive X-ray spectroscopy (EDX). TEM measurements were performed with two different microscopes. The first was a Philips CM30ST (300 kV, LaB_6 cathode) equipped with a Spinning Star device (Nanomegas) for applying precession electron diffraction (PED, maximum precession angle: 3°). EDX was performed in the scanning- and nanoprobe mode of CM30ST with a Si/Li-EDX detector (Noran, Vantage System). The samples were placed on alumina grids, which were fixed in a side-entry, double-tilt holder with the tilting limited to a maximum of ± 25° in two directions. The second TEM was a Tecnai G^2 F30 S-TWIN (300 kV, FEG) equipped with a Si/Li-EDX detector (EDAX). Samples were placed on molybdenum grids, fixed in a double-tilt holder.

The optical bandgap of the materials was determined using the Kubelka-Munk method. For this purpose, UV/Vis reflection spectra were measured with a Cary5 Varian Techtron UV/Vis/NIR spectrometer, operating in the spectral range of 200–3300 nm with 0.05 nm resolution.

Results and Discussion

Morphology and Composition of the Materials

Solvothermal syntheses were performed with Cu:In:S ratios 1.3:5:X with X ranging from 8 to 9.5. The excess of sulfur was necessary because sulfur reacts in basic media to form poylsulfides, thiosulfates, and other S-containing species, thus reducing the available sulfide anions for crystallization of $CuIn_5S_8$. The amount of Cu was selected as 1.3:5:X because it was reported that the growth of Cu-In-S phases occurs via $Cu_{2-x}S$ nanoparticles.[69] At lower S contents a black phase occurred in small quantities, which could be identified as $CuInS_2$ crystallizing in the wurtzite type structure (see TEM analysis). In many products mixtures of three different types of crystals could be observed: black (named C1), orange (named C2), and red (named C3) compounds, with C1 being always present in very small amounts, if observed in the light microscope.

The black component C1 (see Figure 1d) consists of tandems and multiples of aligned plates, indicated by arrows in the SEM micrograph (Figure 1a). This material shows signs of self-organization in needles. Structures of aligned plates are not common, and have been usually observed in biominerals like nacre or in seeded grown crystals.[70] The EDX analysis performed in the TEM on several points of the plates gives the empirical formula $Cu_{1.3(0.11)}InS_{2.26(0.15)}$ (values in parentheses: estimated standard deviations). The EDX data suggests that the composition of C1 is close to $CuInS_2$. Crystals of C2 represent

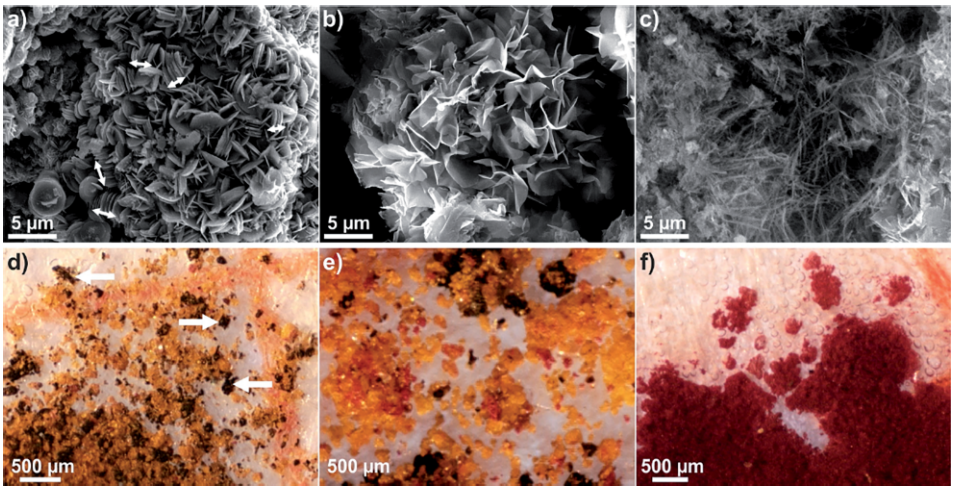

Figure 1. SEM micrographs of the studied species: (a) compound C1 consisting of plate-like crystals with composition $Cu_{1.3(0.11)}InS_{2.26(0.15)}$, marked by white arrows, (b) crystals C2 crystallized as "nanowalls" with composition $CuIn_{2.9(0.09)}S_{5(0.21)}$, and (c) C3 being composed of thin nanobelts with composition $Cu_{1.11(0.38)}In_7S_{10.95(0.9)}$. Light microscopy images: (d) C1 appears as black impurity, (e) orange-colored agglomerates of C2 (main component) and C1, (f) and red C3 which could be prepared as nearly phase pure product.

the predominant phase in the orange component (see Figure 1e), consisting of very thin plates of around 4 µm in lateral dimensions and just a few nanometers thick (Figure 1b). The small thickness appears to be constant over the entire area range. It is noteworthy, that such extreme aspect ratio is only rarely found for layered materials including the well examined metal dichalcogenides. In many instances these plates resemble the petals of a flower, growing from a common point. Some authors refer to thin plates growing over a bulk as "nanowalls",[71,72] therefore the term nanowalls is adopted to describe C2. The empirical formula of this compound is $CuIn_{2.9(0.09)}S_{5(0.21)}$, i.e. very close to $CuIn_3S_5$. The red crystals C3 consist of nanobelts (Figure 1c) and are found in the product of S-rich syntheses after long reaction times (see Figure 1f). According to EDX analysis the empirical chemical formula of the nanobelts is $Cu_{1.11(0.38)}In_7S_{10.95(0.9)}$, i.e., C3 represents a Cu-poor ternary chalcogenide.

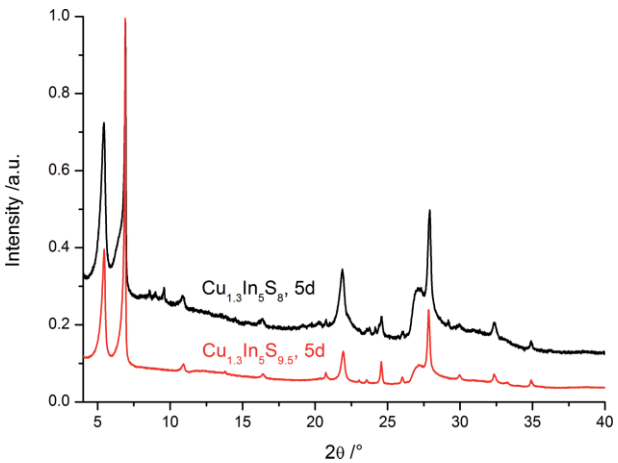

Figure 2. Selected X-ray powder patterns of the products obtained with different ratios of the starting materials after 5 d reaction time. The intensity scale is normalized.

Structural Characteristics

The first syntheses were performed at T = 150–180 °C but the reaction products were mainly amorphous or showed a very low crystallinity. Hence the temperature was increased to T = 220 °C and the reaction time was initially 5 d. In the XRPDs of two selected reaction products the influence of the S-content is obvious (see Figure 2). The XRPD of the sample crystallized from the mixture Cu:In:S = 1.3:5:8 indicates a much less crystalline product and contains more reflections than that measured for 1.3:5:9.5.

The color of the products was red-orange with only a few very small black crystallites. The occurrence of reflections at relatively low scattering angles indicates at least one relatively large lattice parameter. Other features of the XRD patterns are remarkable: the reflections are broad, which is typical for crystallites in the nanoregime; the shape of several Bragg reflections is different and a broad feature is seen at around 27.5° 2θ. These observations suggest that the materials are strongly affected by stacking faults and turbostratic disorder (layers are shifted and rotated against each other), phenomena, which are often observed for layered materials like e.g. graphite, clay minerals or dichalcogenides like MoS_2. The reflections in the X-ray powder pattern are affected by the disorder in different ways: stacking faults lead to a broadening and shift of the reflections; turbostratic disorder does not significantly affect reflections related to the stacking direction of the layers e.g. the 00l series, but reflections of the type $hk0$ and hkl with $l \neq 0$ and h or $k \neq 0$ are significantly broadened. We note that the reflections could not be assigned to any of the known Cu-In-S compounds, but all attempts to index the patterns failed, which can be explained by the pronounced disorder mentioned above.

The influence of the reaction time onto product formation was investigated for Cu:In:S = 1.3:5:8 (Figure 3). In the XRD patterns several remarkable changes are obvious: the intensity ratio of the two intense reflections at low scattering angles is altered and for the sample obtained after 10 d the most intense reflection is that at 5.4° 2θ, while the intensity of the reflection at 6.9° 2θ decreased. In addition, the number of reflections is reduced in the XRDP after 10 d reaction time, while the broad "hump" at about 27.5° 2θ is still visible. Because the most crystalline sample was obtained for $Cu_{1.3}In_5S_{9.5}$ a long term experiment was performed (Figure 4).

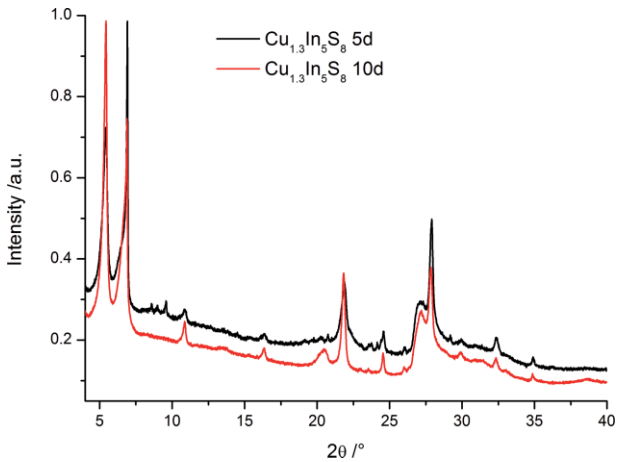

Figure 3. X-ray powder patterns collected for two samples reacted for different times. The intensity scale is normalized.

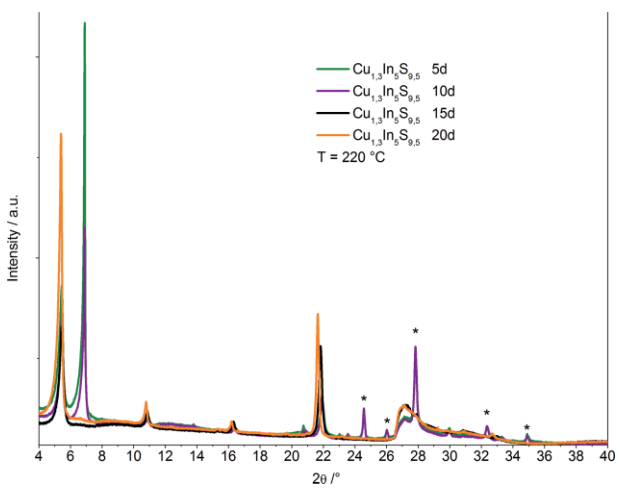

Figure 4. X-ray powder patterns of products obtained after 5 to 20 d reaction time for $Cu_{1.3}In_5S_{9.5}$. Reflections marked with an asterisk: explanation see text.

With increasing reaction time the intensity of the reflection at 6.9° 2θ is reduced and after 15 d this reflection disappeared. Moreover, the relatively sharp reflections marked with an asterisk in Figure 4 all disappeared in the pattern collected after 15/20 d reaction time. The findings may be regarded as a hint that the reflection at 6.9° 2θ and those marked with an asterisk represent a different phase than the remaining reflections. During our search for Cu-In-Q (Q = chalcogen) phases we found the crystal structure of $CuIn_7Se_{11}$ crystallizing in the trigonal space group $P3m1$ with a layered structure (a ≈ 4.036 Å, c ≈ 32.702 Å). The powder pattern is very similar to that observed for the sample $Cu_{1.3}In_5S_{9.5}$ (20 d) and we simulated a diagram using the structural data published in reference[73] (Figure 5). The pronounced preferred orientation of the crystallites was taken into account in the simulation of the pattern. The reflections of the (00l) series match very well with the positions in the calculated pattern assuming c ≈ 16.40 Å, while cross-reflections are hidden under the broad "bump" located between 26.5 and 28.5° 2θ. It is highly likely that the red material is isostructural to $CuIn_7Se_{11}$ because chemical analysis performed in the TEM (EDX, see below) gives as average composition $Cu_{1.11(0.38)}In_7S_{10.95(0.9)}$. This is a new finding, because for $CuIn_7S_{11}$ samples prepared by high temperature synthesis or as films it was reported that the material crystallizes in the cubic space group $Fd3m$ as a defect spinel.

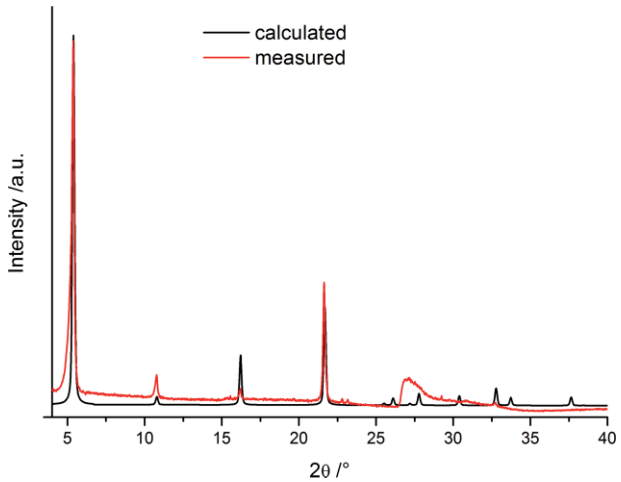

Figure 5. Experimental X-ray powder pattern of $Cu_{1.3}In_5S_{9.5}$ 20d (red) and the calculated pattern based on the structural data of $CuIn_7Se_{11}$.

We note that the color of the products gradually changed from orange to red with increasing reaction time, i.e. it seems that the orange material C2 is a mixture of two compounds. All attempts to synthesize a phase pure compound exhibiting the X-ray powder pattern with only the strong reflection at ca. 6.9° 2θ (and those marked with an asterisk in Figure 4) failed. The X-ray powder patterns recorded for all compounds obtained with different starting material ratios clearly indicate the presence of phase mixtures for reaction times up to 10 d. Only for the largest S content and long reaction times C3 was observed as final product, and C2 may be regarded as an intermediate on the way for formation of C3. To gain information about the structure of C2 HRTEM and EDX analyses were performed (see below).

High Resolution Transmission Electron Microscopy

Because not enough material of the black component C1 could be manually separated for collecting a suitable X-ray powder pattern, TEM investigations were performed on selected round plates with diameters of about 5 µm, which are

commonly stacked, but sometimes it was possible to find isolated plates. The HRTEM micrograph of Figure 6a shows a thin region with the composition $CuInS_2$ (EDX: $Cu_{1.00}In_{0.96}S_{2.04}$). The FFT of the HRTEM micrograph (Figure 6b) reveals a sixfold symmetry, which coincides with the experimental and simulated ED pattern for zone axis [001] of wurtzite type $CuInS_2$ (cf. Figure 6c and Figure 6d, respectively). The reported *d* value for (010) is 3.38 Å,[18] while the average experimental value amounts 3.40 Å.

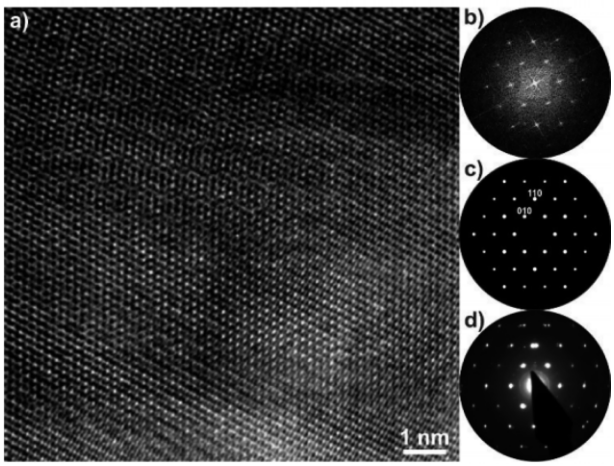

Figure 6. (a) Fourier filtered HRTEM micrograph from C1 with (b) FFT image. The ED pattern (d) from the same region confirms the presence of C1. It matches to the simulated ED pattern (c) of wurtzite type $CuInS_2$ along zone axis [001]. The measured ED pattern (d), is also consistent with (a) and (b).

As mentioned above in many products of the syntheses, C2 and C3 are observed in orange-red agglomerates, and a manual separation of C2 from C3 was not possible. Crystals of C2 were identified in the TEM as very thin plates highly transparent to the electron beam over the entire area range even in SEM mode. In contrast to the wedge shape of bulk crystals, the thickness of the nanowalls appears constant within micron-size areas by the constant bright- or dark field contrast suggesting the presence of an ultra-thin few-layer material. These plates may be regarded as nanowalls that show a clear tendency to roll up (Figure 7). The rolling axis is indicated with an arrow in the micrograph (Figure 7a). Curved surfaces of the nanowalls present strong fluctuations of the high resolution contrast (cf. Figure 8). The diffuse streaks intersecting in 000 in the FFT of this micrograph (Figure 8c upper right) suggest that the rolled nanowall contains in-plane defects. This finding is supported by the parallel stripes seen in the HRTEM micrograph.

Figure 8a shows a HRTEM micrograph of a top view of a nanowall with good crystalline quality. The FFT of this image (Figure 8 upper right) evidences a hexagonal symmetry of the structure in the direction perpendicular to the basal plane of the nanowalls. However, the reflection intensity distribution in the PED pattern (Figure 9a) recorded on the same nanowall violates the hexagonal symmetry, probably due to the amount of defects originated by the rolling up.

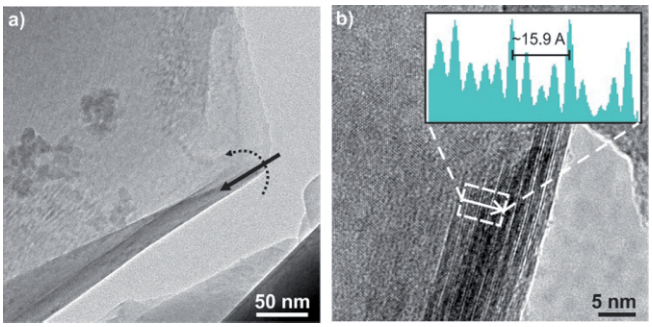

Figure 7. (a) Bending at an edge of nanostacks of component C2 with rolling axis indicated by an arrow. (b) Corresponding HRTEM micrograph with embedded contrast linescan displaying the layer distance of C2.

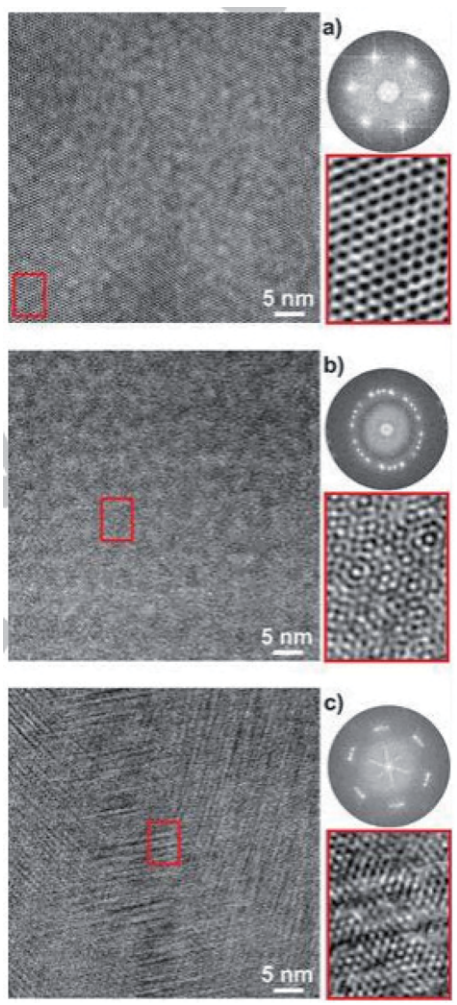

Figure 8. Each left: HRTEM micrographs of C2, each right: attached Fourier transform and enlarged sections from the rectangular areas. (a) Larger perfectly crystalline area as indicted by hexagonal spot pattern. (b) Selected area with several rotated stacks (note the oval appearance of the Fourier transform due to significant deviation from the hexagonal axis). The HRTEM contrast is coined by complex superposition phenomena, (c) Selected area with rotation of stacks and in-plane defects (note the diffuse streaks cutting reciprocal space center within the Fourier transform).

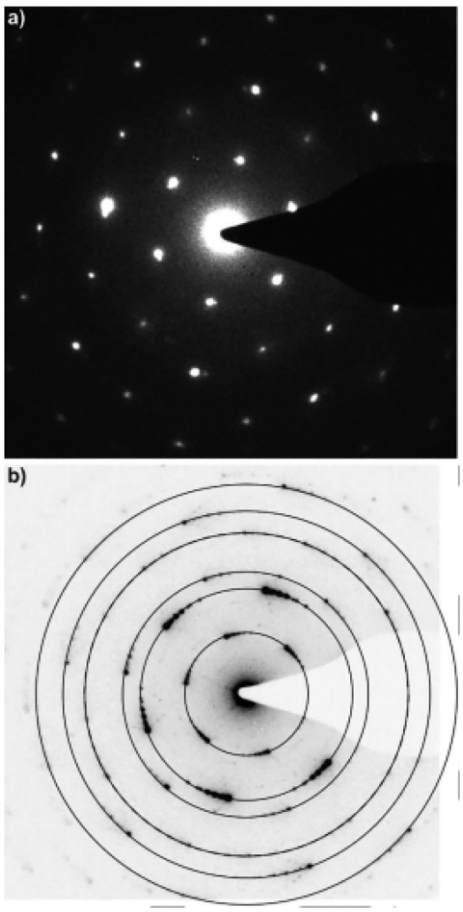

Figure 9. (a) PED pattern recorded on a flat zone of a nanowall of compound C2. (b) Typical SAED pattern of rolled nanowalls of C2. A rotational disorder of consecutive thin layers stacked along the zone axis can be identified. Thus the nanowalls consist of stacked nanometric layers. The pattern describes circles that are assigned to the different planes of C2.

Additionally, SAED patterns recorded on many nanowalls (e.g. Figure 9b) also point to a second feature of the real structure, namely a rotational disorder of consecutive thin layers stacked along the zone axis. Earlier studies on Montmorillonite[74] reported similar features resulting from both, correlated and uncorrelated stacking. Further localized sheet bending in different orientations was investigated by HRTEM, which also occurred for C1 (see Figure 6). Thus the C2 nanowalls consist of stacked nanometric layers indicating that the compound adopts a layered structure. Different from the case of Montmorillonite, the bending of C2 showed a preferred orientation as the layers tend to roll up (Figure 7a). This correlates with a preferably small rotation angle between the stacked layers, indicated by a gap in the ED pattern rings (Figure 9b).

The rotation angles are frequently random, but in many instances, when the thickness is restricted to a few rotated stacks, it is possible to determine the rotation angles and the number of rotated stacks establishing the nanowall. The *d* values of the structure of C2 obtained from the circles of the SAED pattern are 3.29, 1.92, 1.66, 1.26, 1.11, and 0.97 Å and were as well determined by PD experiments. In case of large rotation angles of a few monolayers in the nanowall, fascinating superposition micrographs are recorded (Figure 10). The arrangement of the dots highlights the non-periodic appearance of the superposition, and the composite nature of four rotated layers is clearly seen in the FFT of the micrograph (Figure 10b). The low thickness of the stacks is well supported by the absence of dynamic scattering in the electron diffraction pattern. Thus by nearly kinematic intensity data it could be possible to count the number of layer stacks as each set of reflections can be assigned to one of the rotationally disordered stacks (see the FFT in Figure 10c). This advanced option is part of future work on layered chalcogenides and ferricrystalline materials.[75]

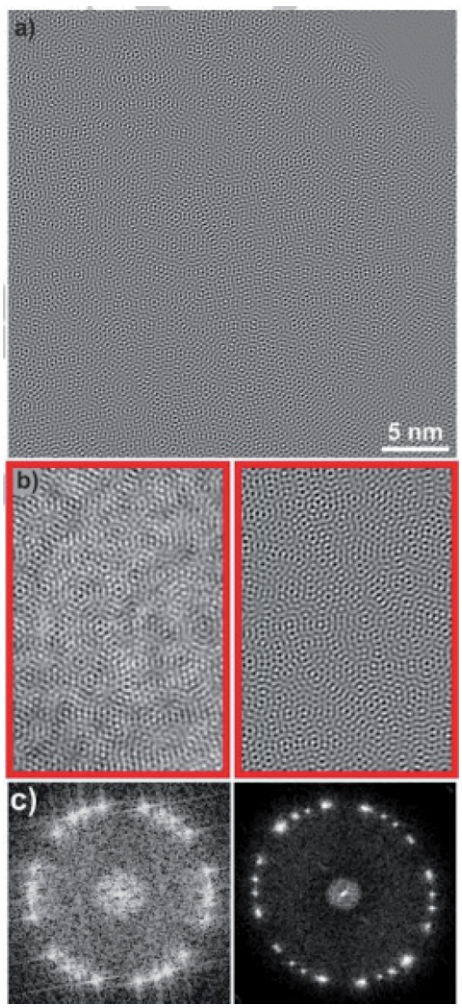

Figure 10. (a) HRTEM imaging on rotationally disordered stacks of C2 (aligned close to hexagonal axis). (b) Left: rationalization of the superposition contrast by superimposing four simulated micrographs which were rotated to each other by 8°, 20°, and 48°, respectively. Right: enlarged section of experimentally observed superposition contrast. (c) Fourier transforms of square selected areas of the images shown in (b).

The analysis indicates that C2 may present a new structural modification, unknown for a Cu-In-S compound with composition close to $CuIn_3S_5$. In previous works $CuIn_3S_5$ has been detected as segregation in $CuInS_2$ prepared with excess of In,[76] but its crystal structure is not exactly known. The prepa-

ration of powders with composition $CuIn_3S_5$ was reported, and a chalcopyrite type structure with space group $P\bar{4}2c$ was proposed with lattice parameters a = 5.82 Å and c = 11.58 Å;[29,31] however, for C2 we can definitely exclude this structure model. Unfortunately, no further structural details were mentioned and the assumptions were not verified e.g. by Rietveld refinements of the X-ray powder data.

The TEM analysis of C3 demonstrates that it is composed of aggregates of "nanobelts", which are randomly arranged (Figure 11a). The average diameter of the single nanobelts is about 20 nm and the lengths vary up to more than 1 µm. The crystallinity of the nanobelts is low and crystal defects are present in the most of them. However, in some cases several aspects of the atomic structure could be determined, for example, the d-values of the structure can be calculated from the rings' radii in the SAED patterns (Figure 11b). On the other hand, the observations with HRTEM (Figure 11c) suggest the formation of strings along the axis of the belts. In all cases the repeating unit perpendicular to the axis was about 12.5 Å estimated from the FFT.

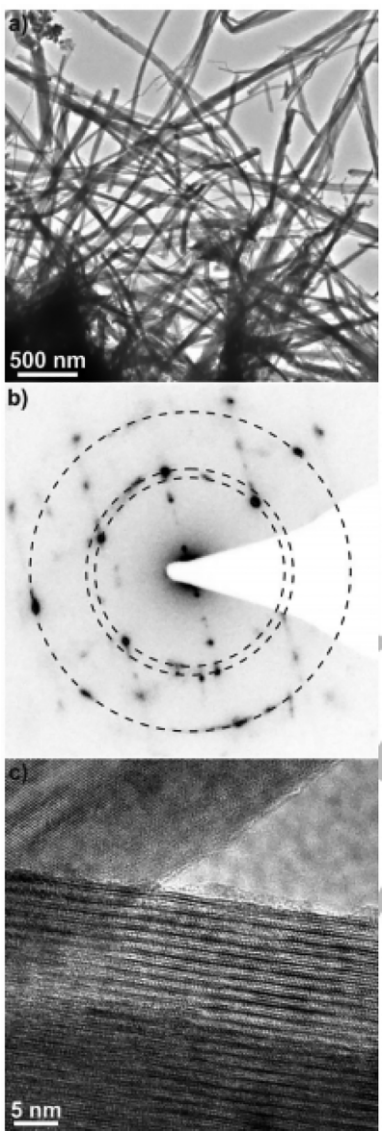

Figure 11. (a)TEM bright field micrograph of C3 (nanobelts). (b) Typical SAED pattern of C3. The nanobelts present prominent structural defects, but it is possible to calculate the d values from the identified rings of the pattern. (c) HRTEM micrographs of a nanobelt of compound C3. The repeated unit perpendicular to the axis of the belts is about 12.5 Å.

The analysis of the three different constituents yields a comprehensive picture of the morphology and composition. The evaluation of the ED patterns indicates that the d values of C3 do not match with data reported for any Cu-In-S phase. The chemical analysis of component C3 yields the composition $Cu_{1.11(0.38)}In_7S_{10.95(0.9)}$ resembling that of the layered chalcogenide $CuIn_7Se_{11}$.[73] Applying this structure type (after adjusting lattice parameters) a good agreement is observed for simulated and experimental X-ray data.

Optical Properties

The red-orange product consisting of C2 and C3 and the phase pure red sample C3 were analyzed with UV/Vis spectroscopy. Applying a Kubelka-Munk plot for determination of the bandgap of the C2/C3 mixture the absorption edges are located at 2.05 and 2.17 eV (Figure 12 top), and for the red compound the bad gap is estimated as 2.05 eV (Figure 12 bottom). These values are larger than that of other Cu-In-S phases (see introduction), but close to that of In_2S_3 (2 eV).[77] But as mentioned in the introduction the bandgap strongly depends on the actual composition and the crystallite sizes.

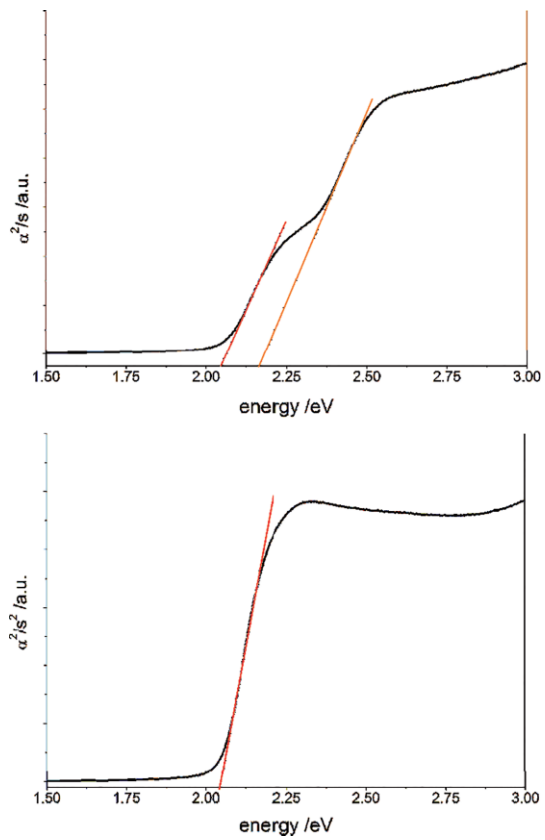

Figure 12. Kubelka-Munk plots of the red-orange component (top) and of the red component C3 (bottom). Note: An intersection with a baseline was considered for the determination of the bandgap.

Conclusions

The reactions of Cu, In, and S in ethylenediamine under solvothermal conditions near the composition Cu:In:S = 1:5:8 led to the formation of three different phases in an intimate mixture. Compound C1 with composition close to $CuInS_2$ is obtained as black piled plates aligned in needles. According to electron diffraction patterns, C1 corresponds to wurtzite-$CuInS_2$. Sample C2 with composition near $CuIn_3S_5$ featured stacked nanowalls with a hexagonal symmetry and the phenomenon of turbostratic disorder. Compound C3 (nanobelts) with an empirical chemical formula $Cu_{1.11(0.38)}In_7S_{10.95(0.9)}$ is a Cu-poor material, which has a laminar structure exhibiting structural similarities to the layered chalcogenide $CuIn_7Se_{11}$. The presented investigations highlight the complexity of solvothermal syntheses, in which product formation depends on several parameters like ratio of starting materials and reaction times. The results show that at short reaction times and lower S contents nucleation and growth of $CuInS_2$ cannot be avoided. With higher S contents and longer reaction times the sample C2 with composition near $CuIn_3S_5$ nucleates and crystallizes together with $CuIn_7S_{11}$. Finally extending the time to 20 d and using an S excess an optically phase pure product could be synthesized. In addition, we have demonstrated that X-ray powder diffractometry is not a conclusive analytical tool for identification of the phases and elaborated HRTEM investigations are necessary to gain more insight into the compositions and structures of the materials.

Acknowledgements

Financial support by the State of Schleswig-Holstein is acknowledged.

Keywords: Solvothermal synthesis; Transmission electron microscopy; X-ray diffraction; Cu-In-S system

References

[1] K. Siemer, J. Klaer, I. Luck, J. Bruns, R. Klenk, D. Bräunig, *Sol. Energy Mater. Sol. Cells* **2001**, *67*, 159–166.
[2] E. Arici, N. S. Sariciftci, D. Meissner, *Adv. Funct. Mater.* **2003**, *13*, 165–171.
[3] R. Klenk, *Thin Solid Films* **2001**, *387*, 135–140.
[4] K. L. Chopra, P. D. Paulson, V. Dutta, *Prog. Photovoltaics* **2004**, *12*, 69–92.
[5] D. H. Jara, S. J. Yoon, K. G. Stamplecoskie, P. V. Kamat, *Chem. Mater.* **2014**, *26*, 7221–7228.
[6] S. Siebentritt, *Thin Solid Films* **2002**, *403–404*, 1–8.
[7] P. V. Kamat, *J. Phys. Chem. Lett.* **2013**, *4*, 908–918.
[8] M. Lv, J. Zhu, Y. Huang, Y. Li, Z. Shao, Y. Xu, S. Dai, *ACS Appl. Mater. Interfaces* **2015**, *7*, 17482–17488.
[9] J. Duan, H. Zhang, Q. Tang, B. he, L. Yu, *J. Mater. Chem. A* **2015**, *3*, 17497–17510.
[10] J. E. Halpert, F. S. F. Morgenstern, B. Ehrler, Y. Vaynzof, D. Credgington, N. C. Greenham, *ACS Nano* **2015**, *9*, 5857–5867.
[11] P. V. Kamat, *Acc. Chem. Res.* **2017**, *50*, 527–531.
[12] J. N. Freitas, A. S. Goncalves, A. N. Nogueira, *Nanoscale* **2014**, *6*, 6371–6397.
[13] J. Kolny-Olesiak, H. Weller, *ACS Appl. Mater. Interfaces* **2013**, *5*, 12221–12237.
[14] K. Zhang, L. Guo, *Catal. Sci. Technol.* **2013**, *3*, 1672–1690.
[15] M. D. Regulacio, M.-Y. Han, *Acc. Chem. Res.* **2016**, *49*, 511–519.
[16] C. Coughlan, M. Ibanez, O. Dobrozhan, A. Singh, A. Cabot, K. M. Ryan, *Chem. Rev.* **2017**, *117*, 5865–6109 and many references therein.
[17] J. J. M. Binsma, L. J. Giling, J. Bloem, *J. Cryst. Growth* **1980**, *50*, 429–436.
[18] Y. Qi, Q. Liu, K. Tang, Z. Liang, Z. Ren, X. Liu, *J. Phys. Chem. C* **2009**, *113*, 3939–3944.
[19] D. Pan, L. An, Z. Sun, W. Hou, Y. Yang, Z. Yang, Y. Lu, *J. Am. Chem. Soc.* **2008**, *130*, 5620–5621.
[20] T. Omata, K. Nose, S. Otsuka-Yao-Matsuo, *J. Appl. Phys.* **2009**, *105*, 073106.
[21] R. Xie, M. Rutherford, X. Peng, *J. Am. Chem. Soc.* **2009**, *131*, 5691–5697.
[22] B. Chen, H. Zhong, W. Zhang, Z. Tan, Y. Li, C. Yu, T. Zhai, Y. Bando, S. Yang, B. Zou, *Adv. Funct. Mater.* **2012**, *22*, 2081–2088.
[23] F. Py, J. Olivier-Fourcade, J. C. Jumas, *J. Solid State Chem.* **1992**, *99*, 319–328.
[24] R. Scheer, H. J. Lewerenz, *J. Vac. Sci. Technol. A* **1994**, *12*, 51–55.
[25] T. Kato, T. Omata, T. Nakamura, D. Anno, Y. Nabetani, T. Matsumoto, *J. Cryst. Growth* **2005**, *275*, e531-e536.
[26] S. Cattarin, P. Guerriero, N. Dietz, H. J. Lewerenz, *Electrochim. Acta* **1994**, *40*, 1041–1049.
[27] B. Berenguier, H. J. Lewerenz, *Electrochem. Commun.* **2006**, *8*, 165–169.
[28] R. Scheer, H. J. Lewerenz, *J. Vac. Sci. Technol. A* **2006**, *24*, 1924.
[29] N. Khemiri, M. Kanzari, *Nucl. Instr. Meth. Phys. Res. B* **2010**, *268*, 268–272.
[30] N. Khemiri, A. Sinaoui, M. Kanzari, *Physica B* **2011**, *406*, 1778–1783.
[31] N. Khemiri, M. Kanzari, *J. Mater. Sci.* **2009**, *44*, 4743–4749.
[32] X. Feng, R. Li, M. Wang, Y. Chen, *J. Mater. Chem. A* **2018**, *6*, 11180–111888.
[33] E. Gastaldi, L. Scaramuzza, *Acta Crystallogr., Sect. B* **1979**, *35*, 2283–3384.
[34] F. Py, M. Womesa, J. M. Durandc, J. Olivier-Fourcade, J. C. Jumas, J. M. Esteva, R. C. Karnatak, *J. Alloys Compds.* **1992**, *178*, 297–304.
[35] S. Kitamura, S. Endo, T. Irie, *J. Phys. Chem. Solids* **1985**, *46*, 881–885.
[36] M. Gannouni, I. Ben Assaker, R. Chtourou, *Int. J. Hydr. Energy* **2015**, *40*, 7252–7259.
[37] M. Gannouni, I. Ben Assaker, R. Chtourou, *Mater. Res. Bull.* **2015**, *61*, 519–527.
[38] I. V. Bodnar, *Semiconductors* **2014**, *48*, 557–561.
[39] N. Khemiri, B. Khalfallah, D. Abdelkader, M. Kanzari, *Int. J. Thin Film. Sci. Tec.* **2014**, *3*, 7–12.
[40] I. V. Bodnar, V. A. Polubok, V. Yu. Rud, Yu. V. Rud, MS Serginov, *Semiconductors* **2004**, *38*, 197.
[41] B. Khalfallah, N. Khemiri, M. Kanzari, *Mater. Sci. Semicond. Proc.* **2014**, *24*, 265–271.
[42] Y. Luo, G. Chang, W. Lu, X. Sun, *Colloid J.* **2010**, *72*, 282–285.
[43] X. Sheng, L. Wang, Y. Luo, D. Yang, *Nanoscale Res. Lett.* **2011**, *6*, 562.
[44] J. Niezgoda, M. Harrison, *Chem. Mater.* **2012**, *24*, 3294–3298.
[45] T. Pons, E. Pic, N. Lequeux, E. Cassette, L. Bezdetnaya, F. Guillemin, F. Marchal, B. Dubertret, *ACS Nano* **2010**, *4*, 2531–2538.
[46] N. Bao, X. Qiu, Y.-H. Wang, Z. Zhou, X. Lu, C. Grimes, A. Gupta, *Chem. Commun.* **2011**, *47*, 9441–9443.
[47] M. Kruszynska, H. Borchert, J. Parisi, J. Kolny-Olesiak, *J. Am. Chem. Soc.* **2010**, *132*, 15976 –15986.
[48] Q. Lu, J. Hu, K. Tang, Y. Qian, G. Zhou, X. Liu, *Inorg. Chem.* **2000**, *39*, 1606–1607.
[49] Y. Cui, J. Ren, G. Chen, Y. Qian, Y. Xie, *Chem. Lett.* **2001**, *2*, 236–237.
[50] W. Du, X. Qian, J. Yin, Q. Gong, *Chem. Eur. J.* **2007**, *13*, 8840–8846.
[51] T.-L. Li, H. Teng, *J. Mater. Chem.* **2010**, *20*, 3656–3664.

[52] W. Yue, S. Han, R. Peng, W. Shen, H. Geng, F. Wu, S. Tao, M. Wang, *J. Mater. Chem.* **2010**, *20*, 7570–7578.
[53] W. Huang, C. Tseng, S. Chang, H. Tuan, C. C. Chiang, L.-M. Lyu, M. H. Huang, *Langmuir* **2012**, *28*, 8496–8501.
[54] S. L. Castro, S. G. Bailey, R. P. Raffaelle, K. K. Banger, A. F. Hepp, *Chem. Mater.* **2003**, *15*, 3142–3147.
[55] D. P. Dutta, G. Sharma, *Mater. Lett.* **2006**, *60*, 2395–2398.
[56] M. Uehara, K. Watanabe, Y. Tajiri, H. Nakamura, H. Maeda, *J. Chem. Phys.* **2008**, *129*, 134709.
[57] S. T. Connor, C.-M. Hsu, B. D. Weil, S. Aloni, Y. Cui, *J. Am. Chem. Soc.* **2009**, *131*, 4962–4966.
[58] D. Deng, Y. Chen, J. Cao, J. Tian, Z. Qian, S. Achilefu, Y. Gu, *Chem. Mater.* **2012**, *24*, 3029–3037.
[59] S. K. Batabyal, L. Tian, N. Venkatram, W. Ji, J. J. Vittal, *J. Phys. Chem. C* **2009**, *113*, 15037–15042.
[60] B. Koo, R. N. Patel, B. A. Korgel, *Chem. Mater.* **2009**, *21*, 1962–1966.
[61] W. Yue, S. Han, R. Peng, W. Shen, H. Geng, F. Wu, S. Taoe, M. Wang, *J. Mater. Chem.* **2010**, *20*, 7570–7578.
[62] S. L. Castro, S. G. Bailey, R. P. Raffaelle, K. K. Banger, A. F. Hepp, *J. Phys. Chem. B* **2004**, *108*, 12429–12435.
[63] H. Nakamura, W. Kato, M. Uehara, K. Nose, T. Omata, S. Otsuka-Yao-Matsuo, M. Miyazaki, H. Maeda, *Chem. Mater.* **2006**, *18*, 3330–3335.
[64] W.-S. Song, J.-H. Kim, J.-H. Lee, H.-S. Lee, Y. R. Do, H. Yang, *J. Mater. Chem.* **2012**, *22*, 21901–21908.
[65] D. Aldakov, A. Lefrançois, P. Reiss, *J. Mater. Chem. C* **2013**, *1*, 3756–3776.
[66] Y. Jiang, Y. Wu, X. Mo, W. Yu, Y. Xie, Y. Qian, *Inorg. Chem.* **2000**, *39*, 2964–2965.
[67] R. H. Arntson, F. W. Dickson, G. Tunell, *Am. J. Sci.* **1960**, *258*, 574–582.
[68] W. F. Giggenbach, *Inorg. Chem.* **1974**, *13*, 1724–1730.
[69] J. Li, M. Bloemen, J. Parisi, J. Kolny-Olesiak, *ACS Appl. Mater. Interfaces* **2014**, *6*, 20535–20543.
[70] Z. R. Tian, J. A. Voigt, J. Liu, B. Mckenzie, M. J. Mcdermott, M. A. Rodriguez, H. Konishi, H. Xu, *Nat. Mater.* **2003**, *2*, 821–826.
[71] C. N. R. Rao, V. V. Agrawal, K. Biswas, U. K. Gautam, M. Ghosh, A. Govindaraj, G. U. Kulkarni, K. P. Kalyanikutty, K. Sardar, S. R. C. Vivekchand, *Pure Appl. Chem.* **2006**, *78*, 1619–1650.
[72] U. K. Gautam, S. R. C. Vivekchand, A. Govindaraj, C. N. R. Rao, *Chem. Commun.* **2005**, 3995–3997.
[73] L. D. Gulay, I. A. Ivashchenko, O. F. Zmiy, I. D. Olekseyuk, *J. Alloys Compds.* **2004**, *384*, 121–124.
[74] L. F. Drummy, H. Koerner, K. Farmer, A. Tan, B. L. Farmer, R. A. Vaia, *J. Phys. Chem. B* **2005**, *109*, 17868–17878.
[75] N. S. Gunning, T. Dankwort, M. Falmbigl, U. Ross, G. Mitchson, D. M. Hamann, A. Lotnyk, L. Kienle, D. C. Johnson, *Chem. Mater.* **2017**, *29*, 8292–8298.
[76] R. Scheer, H. J. Lewerenz, *J. Vac. Sci. Technol. Vac. Surf. Films* **1995**, *13*, 1924–1929.
[77] W. Rehwald, G. Harbeke, *J. Phys. Chem. Solids* **1965**, *26*, 1309–1324.

Received: September 28, 2018
Published Online: January 23, 2019

